Dynamic minimization of proteome reallocation explains metabolic transition in hierarchical utilization of mixed carbon sources

Zhihao Liu[1,2], Minghao Chen[1], Jingmin Hu[1], Yonghong Wang[1*], Yu Chen[2*]

1 State Key Laboratory of Bioreactor Engineering, East China University of Science and Technology, Shanghai 200237, China

2 Key Laboratory of Quantitative Synthetic Biology, Shenzhen Institute of Synthetic Biology, Shenzhen Institute of Advanced Technology, Chinese Academy of Sciences, Shenzhen 518055, China

* Corresponding authors:

Yonghong Wang (yhwang@ecust.edu.cn)

Yu Chen (y.chen3@siat.ac.cn)

Keywords: enzyme constraint, metabolic model, mixed carbon sources, metabolic transition

Abstract

Cells choose between alternative pathways in metabolic networks under diverse environmental conditions, but the principles governing the choice are insufficiently understood, especially in response to dynamically changing conditions. Here we observed that a lactic acid bacterium *Bacillus coagulans* displayed homolactic fermentation on glucose or trehalose as the sole carbon source, but transitioned from homolactic to heterolactic fermentation during the hierarchical utilization of glucose and trehalose when growing on the mixture. We simulated the observation by dynamic minimization of reallocation of proteome (dMORP) using an enzyme-constrained genome-scale metabolic model of *B. coagulans*, which coincided with our multi-omics data. Moreover, we evolved strains to co-utilize mixed carbon sources, circumventing the hierarchical utilization and inactivating the choice of heterolactic fermentation. Altogether, the findings suggest that upon rapid environmental changes bacteria tend to minimize proteome reallocation and accordingly adjust metabolism, and dMORP would be useful in simulating and understanding cellular dynamics.

Introduction

Cells have alternative pathways, i.e., redundancy, in metabolic networks to adapt to diverse environmental conditions. For instance, while many microbes and mammalian cells use respiration for ATP production, some of them also harbor fermentation as an alternative ATP-producing pathway, which enables not only survival under anaerobic conditions but also fast growth in the presence of oxygen, i.e., aerobic fermentation (1). The alternative pathways empower cells to choose between distinct metabolic strategies, but the principles governing the cellular choice are insufficiently understood (2-4).

Experimental and theoretical studies suggest that the choices of alternative pathways and metabolic strategies reflect tradeoffs, mostly between metabolic efficiency, e.g., yield, of pathways and cellular resources, e.g., proteome, invested for enzymes of the pathways (5-9). For instance, fermentation has a lower ATP yield but is more proteome efficient than respiration, and therefore favors fast-growing cells subject to the limited proteome resources (2,10). These studies are predominantly focused on steady-state cultures, e.g., chemostats, of model microbes, and therefore the cellular choice might be a result of a relatively long-term adaption to the environment. However, much less is known whether and how cells can transition between alternative pathways under dynamically changing environments, which are ubiquitous in both natural and artificial biological systems (11).

Here we studied a lactic acid bacterium *Bacillus coagulans*, which has alternative pathways converting glycolytic carbon sources to lactate, i.e., homolactic and heterolactic fermentation (12,13). The former converts carbon sources to lactate via the Embden–Meyerhof–Parnas (EMP) pathway, while the later the phosphoketolase pathway with a lower lactate yield (14,15). We observed that *B. coagulans* displayed the homolactic fermentation on glucose or trehalose as the sole carbon source, but transitioned from homolactic to heterolactic fermentation in the hierarchical utilization of glucose and trehalose when growing on the mixture. We hypothesized that the metabolic transition could be interpreted by dynamic minimization of reallocation of proteome, and performed enzyme-constrained metabolic modeling and multi-omics analysis to test the hypothesis. Finally, by adaptive laboratory evolution (ALE) we evolved strains that can co-utilize the mixed carbon sources, inactivating the heterolactic fermentation.

Results

Lactate yield significantly changed in hierarchical utilization of glucose and trehalose

B. coagulans is widely used in the industrial lactate fermentation (13,16,17), where hydrolysates of low-cost starch-based materials are commonly used as the carbon sources (18,19) considering cost and benefit. However, the co-existence of multiple carbon sources in the medium may lead to the hierarchical utilization (20-25) and thus the waste of substrates (26), the extension of fermentation cycle (27) and the difficulty in product separation and purification (28). Therefore, identifying the principles governing the dynamic behavior of *B. coagulans* during the hierarchical

utilization of mixed carbon sources would be of significance from both basic and applied science perspectives.

We performed batch fermentation of *B. coagulans* on the mixture of glucose and trehalose, a disaccharide with a high percentage in the hydrolysates (29). We observed the hierarchical utilization of glucose and trehalose, which divided the entire fermentation process into three phases (Fig. 1A). In the glucose utilization phase (P_{gluc}, 0-12 h), glucose was exclusively consumed and lactate was rapidly produced with the lactate yield on glucose reaching as high as 0.897 g/g, which was similar to the yield (i.e., 0.882 g/g) on glucose as the sole carbon source (Fig. 1B) and close to the yield of homolactic fermentation (14,30). Upon glucose depletion, the lag phase occurred (P_{lag}, 12-16 h), in which the lactate production stopped, the biomass concentration (measured by OD620) declined (Fig. 1A) and a few organic acids were slightly consumed (SI Appendix Fig. S1). In the trehalose utilization phase (P_{tre}, 16-84 h), trehalose was consumed, and lactate was produced again (Fig. 1A). Interestingly, the lactate yield on trehalose in P_{tre} was only 0.526 g/g, which was much lower than that (i.e., 0.851 g/g) on trehalose as the sole substrate (Fig. 1B) and close to the theoretical lactate yield of heterolactic fermentation (14). This was in line with the increased yields of byproducts in P_{tre} (SI Appendix Table S1). The significant change in the lactate yield during the hierarchical utilization of glucose and trehalose indicated distinct strategies to catabolize the carbon sources in P_{gluc} and P_{tre}.

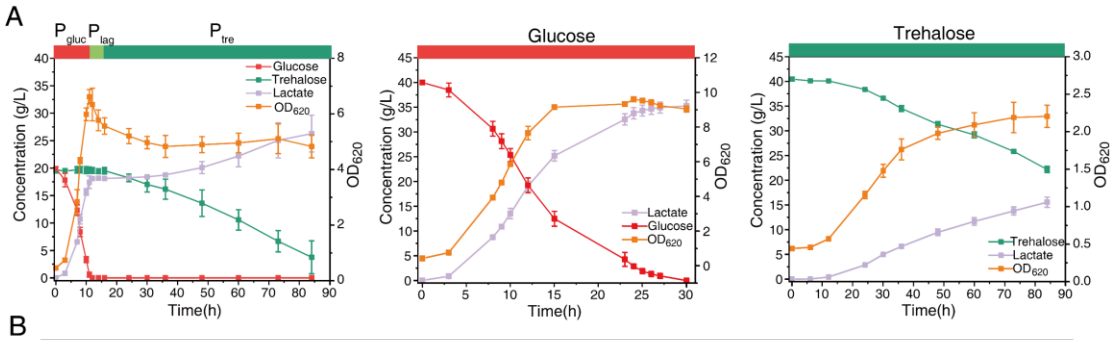

B

Carbon source conditions	P_{gluc}	P_{tre}	Glucose	Trehalose
Lactate yield (g/g)	0.897±0.015	0.526±0.041	0.882±0.006	0.851±0.044

Figure 1. Fermentation results on various carbon sources in 5 L bioreactor by *B. coagulans*. (A) Fermentation processes on the combination of glucose and trehalose as the mixed carbon sources (left), sole glucose (middle) and sole trehalose (right). Data in the plots are shown with mean ± s.d. of three biologically replicates. (B) Lactate yields under various carbon source phases or conditions. Data in the table are shown with mean ± s.d. of three biologically replicates.

Dynamic minimization of reallocation of proteome captured metabolic changes

To gain a systematic understanding, we reconstructed a genome-scale metabolic model of the strain *B. coagulans* DSM 1 = ATCC 7050 (31) called iBcoa620, which was evaluated by the Memote score (32) and validated by growth on various carbon sources (SI Appendix Fig. S2). Subsequently, we converted iBcoa620 into an enzyme-constrained version eciBcoa620 using the GECKO toolbox

(33), allowing for understanding of metabolic changes by taking into account the enzyme usage and proteome allocation.

To simulate the changes during the fermentation process, we performed dynamic flux balance analysis (dFBA) (34) with eciBcoa620 (Fig. 2A). The dFBA approach can divide the entire period into multiple time intervals and obtain the flux distribution at each time interval by performing classical FBA (35) which requires a predefined objective function. While growth maximization appeared reasonable to simulate each time intervals in P_{gluc}, it could not predict the cellular behavior accurately after glucose depletion (Fig. 2B), meaning that cells adjusted the objective in response to the changing environment. Therefore, we attempted other commonly used objective functions (36), including to maximize lactate production and to maximize non-growth-associated maintenance (NGAM), and found that they also failed to capture the cellular behavior in P_{tre} (SI Appendix Fig. S3), i.e., the former predicted much higher lactate production while the latter no lactate production (Fig. 2B).

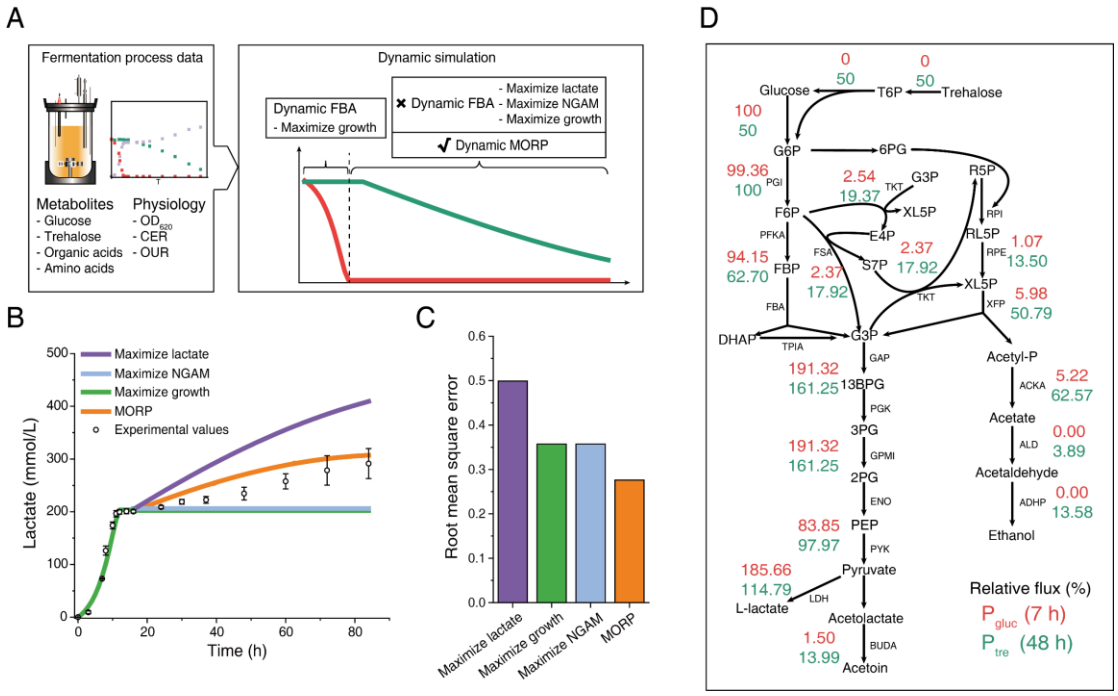

Figure 2. Simulation of batch fermentation under mixed carbon sources by eciBcoa620. (A) Dynamic simulation of the fermentation process. In the dFBA simulation of P_{gluc} the growth rate was maximized. To simulate P_{tre}, various objective functions could be adopted within the dFBA framework. Additionally, we developed an approach to dynamically minimize the proteome reallocation with the enzyme-constrained models. (B) Simulation of lactate production using different objective functions. Minimization of proteome reallocation predicted the lactate production in P_{tre} better compared to the others. Data in the plot are shown with mean ± s.d. of three biologically replicates. (C) Root mean square errors of the different objective functions in predicting P_{tre}. Root mean square error quantifies the difference between the predicted and experimental fluxes. The predicted fluxes refer to the production fluxes of organic acids in all simulation steps in P_{tre}, while

the experimental fluxes refer to the values obtained by fitting the detected organic acid concentrations in P_{tre}. (D) Comparison of the relative fluxes of the central carbon metabolism (CCM) between P_{gluc} (represented by 7 h) and P_{tre} (represented by 48h). Relative flux is calculated as the percentage of the absolute flux of each reaction to the uptake flux of the substrates. Note that one unit of trehalose uptake flux was converted to two unit of glucose uptake flux. T6P, trehalose 6‐phosphate; G6P, glucose 6‐phosphate; F6P, fructose 6‐phosphate; FBP, fructose 1,6‐bisphosphate; DHAP, dihydroxyacetone phosphate; G3P, glyceraldehyde 3‐phosphate; 13BPG, glycerate 1,3‐bisphosphate; 3PG, 3-phosphoglycerate; 2PG, 2-Phospho-D-glycerate; PEP, phosphoenolpyruvate; 6PG, gluconate 6‐phosphate; E4P, erythrose 4‐phosphate; S7P, sedoheptulose 7-phosphate; R5P, ribose 5‐phosphate; RL5P, ribulose 5‐phosphate; XL5P, xylulose 5-phosphate; Acetyl-P, Acetyl phosphate; PGI, glucose-6-phosphate isomerase; PKFA, 6-phosphofructokinase; FBA, fructose-1,6-bisphosphate aldolase; GAP, glyceraldehyde-3-phosphate dehydrogenase; PGK, phosphoglycerate kinase; GPMI, phosphoglycerate mutase; ENO, enolase; PYK, pyruvate kinase; LDH, L-lactate dehydrogenase; RPI, ribose 5-phosphate isomerase; RPE, ribulose-phosphate 3-epimerase; XFP, phosphoketolase; FSA, fructose-6-phosphate aldolase; TKT, transketolase; BUDA, acetolactate decarboxylase; ACKA, acetate kinase; ALD, aldehyde dehydrogenase; ADHP, alcohol dehydrogenase.

Considering the fact that proteome reallocation requires frequent protein synthesis and degradation, which is of high cost to cells (37), we hypothesized that cells tend to dynamically minimize the proteome reallocation in response to rapid environmental changes. To test it, we developed the approach of dynamic minimization of reallocation of proteome (dMORP) to simulate the cellular behavior after glucose depletion (Fig. 2A). The approach leverages the enzyme-constrained models, which enable explicit calculation of enzyme usage, and minimizes the sum of absolute differences of all enzyme usage values between previous and current time intervals (Materials and methods). By employing dMORP, we found that the lactate production in P_{tre} was well predicted (Fig. 2B). Moreover, dMORP outperformed other tested objective functions as it led to the smallest Root Mean Square Error (RMSE) (Fig. 2C) and it was capable of predicting production of byproducts in P_{tre} such as acetate and acetoin (SI Appendix Fig. S3). Therefore, we demonstrated that dynamic minimization of proteome reallocation could be a more realistic objective function for describing the cellular behavior after glucose depletion.

Inspection of the simulated flux distributions enabled us to explain the observed lower lactate yield in P_{tre}. We compared the relative fluxes, i.e., normalized to carbon source uptake, of the central carbon metabolism (CCM) in P_{tre} (simulated at 48 h, i.e., middle in P_{tre}) to those in P_{gluc} (simulated at 7 h, i.e., mid-exponential phase in P_{gluc}) and identified in P_{tre} a much greater fraction of carbon flux toward the key reaction of heterolactic fermentation phosphoketolase (Fig. 2D) as well as related reactions such as ribulose-phosphate 3-epimerase and acetate kinase, resulting in carbon loss in the form of acetate and ethanol and thereby the decreased lactate yield (13). This was also in line with the comparison between P_{tre} and the sole trehalose condition (SI Appendix Fig. S4).

To compare the metabolic changes between different phases during the hierarchical utilization of glucose and trehalose, we selected the absolute metabolic fluxes simulated at 7 h, 14 h and 48 h,

representing P_{gluc}, P_{lag} and P_{tre}, respectively (Fig. 3A). We found that the metabolic fluxes in P_{lag} and P_{tre} were comparable but generally less than those in P_{gluc} (Fig. 3A), exemplified by the lower glycolytic fluxes, which was due to the considerably slower substrate uptake (Fig. 1A). Interestingly, in order to dynamically minimize the proteome reallocation after glucose depletion, the model predicted high fluxes through both forward and backward directions for some reversible reactions in the glycolysis pathway (Fig. 3A), which minimized the reduction in the enzyme usage meanwhile allowed for a sharply decrease in the net flux. Such high fluxes through both reaction directions might suggest the control of reaction thermodynamics on fluxes as reported previously (38-41). Additionally, we found in the comparison between P_{gluc} and P_{tre} that the reactions phosphoketolase, ribulose-phosphate 3-epimerase and acetate kinase displayed smaller changes in fluxes than glycolytic reactions (SI Appendix Fig. S5), which ensured an enhanced flux fraction in response to a large reduction in the substrate uptake flux, indicating their essential contribution to heterolactic fermentation, i.e., the low lactate yield.

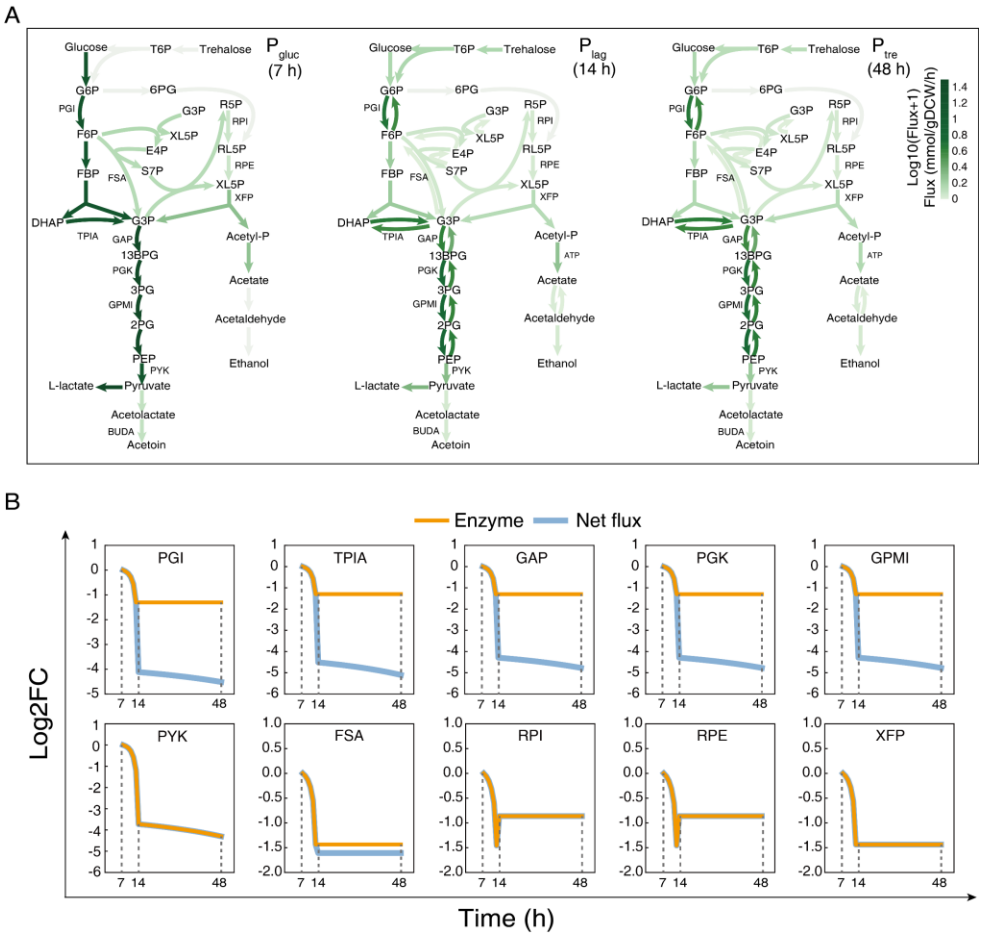

Figure 3. Dynamical changes in metabolic fluxes and enzyme usage in the fermentation process predicted by eciBcoa620. (A) The absolute metabolic flux distributions of the CCM at 7 h, 14 h, and 48 h. These three time points represent P_{gluc}, P_{lag} and P_{tre}, respectively. At 7 h the objective function was to maximize growth while at 14 h and 48 h it was to minimize proteome

reallocation. (B) Enzymes usage and net fluxes of the central carbon metabolism from 7 h to 48 h. The log2FC value represents the change in enzyme usage or net flux relative to the 7 h point.

The enzyme-constrained model allowed us to investigate the enzyme usage under each time interval. By plotting the change in enzyme usage versus fermentation time we found that the enzyme usage remained almost constant after glucose depletion at 12 h (Fig. 3B), indicating the effectiveness of the minimization of proteome reallocation between adjacent time intervals. We also noticed that while the change in fluxes kept in step with the change in enzyme usage for reactions like phosphoketolase, many glycolytic enzymes displayed tremendous difference between changes in fluxes and changes in enzyme usage in P_{lag} and P_{tre} (Fig. 3B), which could be explained by their elevated reverse fluxes (Fig. 3A). This may also indicate the control of metabolites, rather than gene expression, over glycolytic fluxes (42).

To compare with the dMORP approach, we examined the simulations performed using lactate production maximization as the objective function in a dynamic manner (Fig. 2B, SI Appendix Fig. S6). As expected the simulated flux distribution at 48 h displayed homolactic fermentation, i.e., trehalose was mostly converted to lactate without acetate production (SI Appendix Fig. S6A), inconsistent with the experimental observation (SI Appendix Fig. S1). In addition, we found that the simulated enzyme usage of many reactions, e.g., glycolytic reactions, altered much more considerably compared with the simulations using dMORP (SI Appendix Fig. S6B).

Multi-omics data coincided with dynamic minimization of proteome reallocation

To validate our hypothesis, we collected transcriptomics and proteomics data at 7 h, 14 h and 48 h, representing P_{gluc}, P_{lag} and P_{tre}, respectively. The transcriptomics and proteomics data showed high consistency among biological triplicates while clear variability among different phases (SI Appendix Fig. S7). Based on the data, we mapped changes in mRNA and protein levels between phases onto the CCM (Fig. 4A). By comparing P_{tre} versus P_{gluc}, we found that most reactions in the glycolysis and phosphoketolase pathway were slightly downregulated (Fig. 4A) as the changes in mRNA and protein levels were either subtle or not significant (SI Appendix Table S2). This is in line with the changes in the enzyme usage simulated by the model with dMORP (Fig. 3B), rather than those with maximizing lactate production (SI Appendix Fig. S6B). In addition, the comparison of P_{tre} versus P_{lag} showed subtle, even smaller, changes in the mRNA and protein levels of the glycolysis and phosphoketolase pathway (Fig. 4A, SI Appendix Table S2), as predicted by the model (Fig. 3B). Therefore, the data showed that while the metabolic fluxes altered considerably after glucose depletion (Fig. 3) the gene expression levels did not alter so much as the metabolic fluxes. This indicates that the cellular proteome tends to maintain minimal adjustment upon rapid environmental

changes and that there are other mechanisms than gene expression that might explain the metabolic changes.

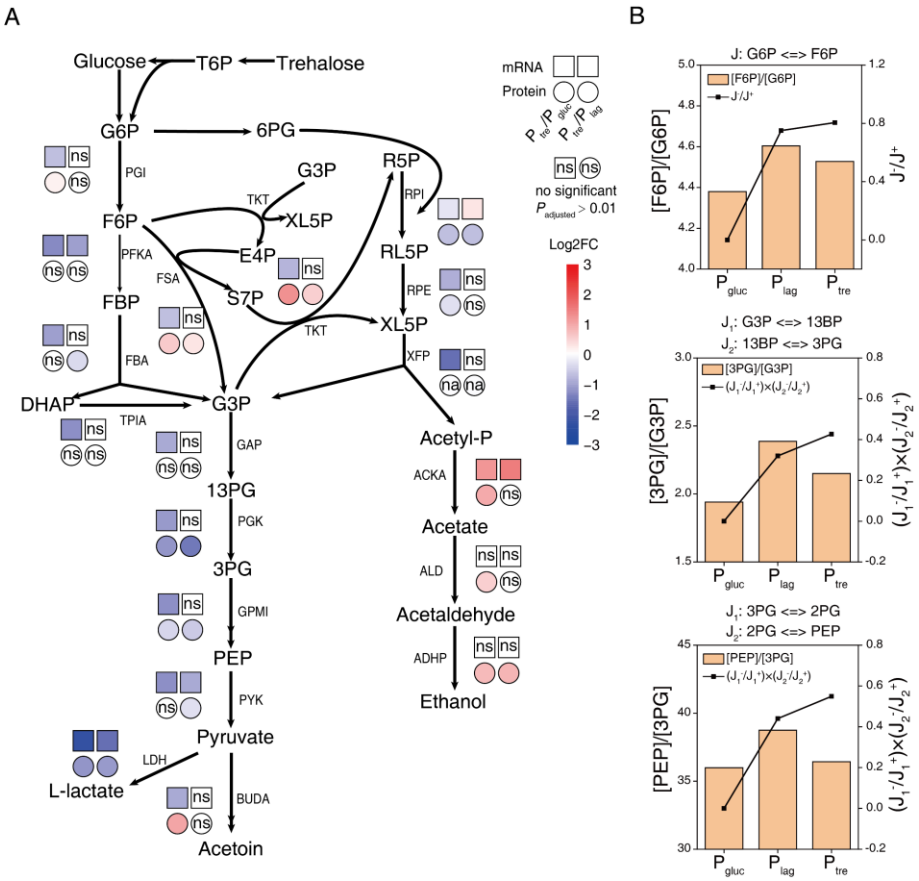

Figure 4. Analysis of transcriptomics, proteomics and intracellular metabolite data. (A) Transcriptomics and proteomics comparison for the CCM between phases. The omics samples of three phases were obtained from three biological replicates, respectively. Significance analysis between two phases were performed using the two-sided *t*-test, and a cut-off adjusted *P* value ($P_{adjusted}$) of 0.01 was adopted. "na" indicates that the data is not available. (B) The comparison between substrate-product concentration ratio and forward-backward flux ratio. "+"and "-" represent the forward and backward flux of the reaction, respectively.

As suggested by the model, the mismatch between the changes in the metabolic fluxes and gene expression levels could be explained by the increased reverse fluxes (Fig. 3). To validate it, we measured intracellular metabolite concentrations at 7 h, 14 h and 48 h, representing P_{gluc}, P_{lag} and P_{tre}, respectively (SI Appendix Fig. S8 and S9). Based on the thermodynamics of reactions (38,43), the ratio of backward over forward flux of a reversible reaction should be proportional to the ratio of product over substrate concentration (SI Appendix Supplementary Note). Due to the limited coverage of the metabolite data, we could only calculate for the reaction glucose-6-phosphate isomerase whose substrate and product were both detected, and found that for this reaction the ratio of measured product over substrate concentration increased after glucose depletion (Fig. 4B), supporting the contribution of the reverse flux. To make full use of the metabolite data, we lumped

a few glycolytic reactions to carry out the calculation and also found a similar trend, i.e., increased ratio of the final product over the substrate concentration (Fig. 4B). It should be noted that the ratio of the product over substrate concentration did not change so significantly as the ratio of the simulated backward over forward flux, which was as expected since the model did not consider the changes in other factors that could regulate metabolic fluxes such as enzyme saturation (43) and enzyme activity (44).

In conclusion, after glucose depletion cells tended to utilize the proteome expressed on glucose to consume trehalose, in which the mismatch between the relatively higher gene expression levels of glycolytic enzymes and the lower glycolytic flux might be contributed by the enhancement of some reverse fluxes as indicated by the metabolite data. In addition, the flux through the phosphoketolase pathway did not decrease so much as the glycolytic flux, which led to an increased fraction of carbon source toward phosphoketolase pathway and thus lowered lactate yield.

Evolved strains performed homolactic fermentation by co-utilizing the mixed carbon sources

Considering that the heterolactic fermentation was triggered by the dynamic switch from glucose to trehalose utilization, we hypothesized that simultaneous utilization of the carbon sources would prevent *B. coagulans* from choosing the heterolactic fermentation. To test it, we carried out ALE (45,46) to obtain strains that could co-utilize glucose and trehalose with improved lactate yield (Fig. 5A) (Materials and methods). As a result, we obtained four evolved strains that can utilize glucose and trehalose simultaneously (SI Appendix Fig. S10), which was further confirmed by the 5 L bioreactor cultivation of one of the evolved strains Ev3 (Fig. 5B). Notably, the evolved strain Ev3

outperformed the wildtype strain in terms of the final lactate titer (35.892 v.s. 26.220 g/L) and the total fermentation time (24 v.s. 84 h) (Fig. 1A & Fig. 5B).

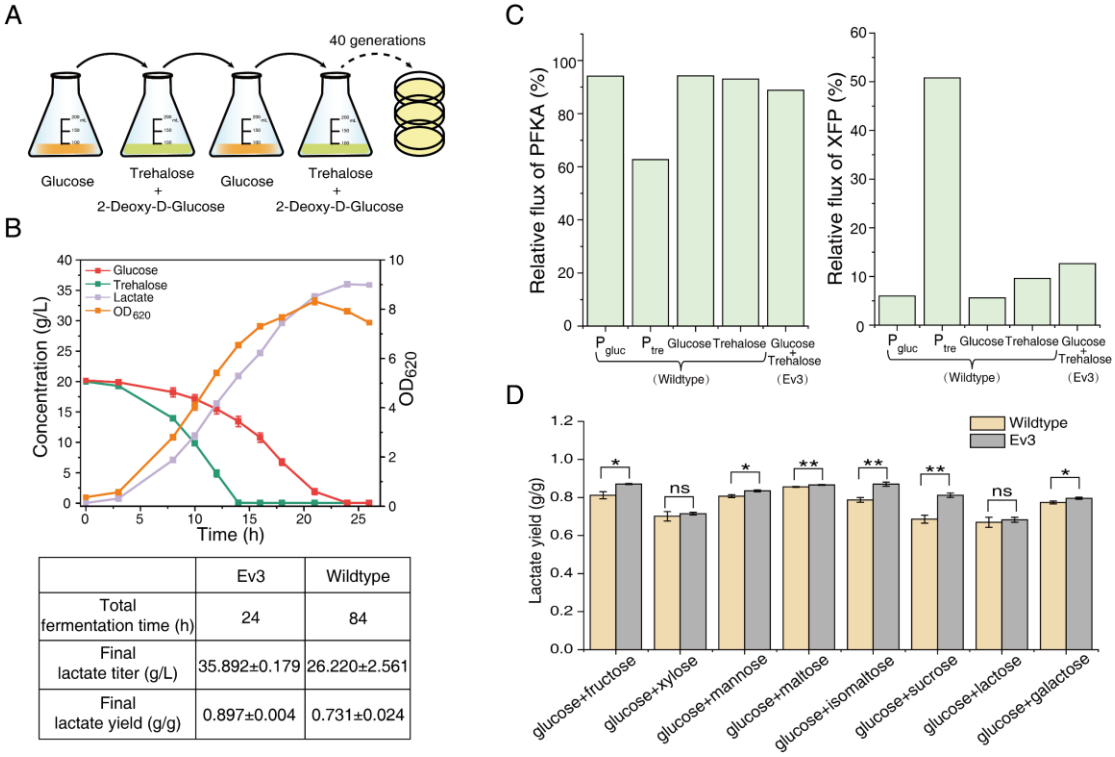

	Ev3	Wildtype
Total fermentation time (h)	24	84
Final lactate titer (g/L)	35.892±0.179	26.220±2.561
Final lactate yield (g/g)	0.897±0.004	0.731±0.024

Figure 5. Adaptive laboratory evolution improved fermentation process. (A) Brief diagram of adaptive laboratory evolution experiment. The addition of 2-Deoxy-D-glucose to trehalose aimed at efficiently utilizing trehalose in the absence of glucose, with the intention of eliminating the catabolite repression effect. After 40 generations, growth and lactate production were basically stable. The strains with notably improved lactate production were selected for subsequent shake flasks validation and 5 L bioreactor experiments. (B) Profiles of fermentation process with mixed carbon sources in 5 L bioreactor by the evolved strain Ev3. Data in the plot are shown with mean ± s.d. of three biologically replicates. (C) Relative fluxes through PFKA and XFP over the substrate uptake fluxes of the evolved strain Ev3 and wildtype strain on different carbon sources. (D) Lactate yields on different pairs of carbon sources of evolved strain and wildtype strain. The cultivation process was carried out in 250 mL shake flasks, with the carbon source concentration of 20 g/L for each. The concentrations of lactate and carbon sources at 36 h were measured to calculate the lactate yields. Data in bar diagram are shown with mean ± s.d. of three biologically replicates. Statistical analysis was performed using two-sided *t*-test. Statistically significant differences are described as follows: ** $P<0.01$, * $P<0.05$, ns (not significant).

The lactate yield of the strain Ev3 on glucose and trehalose (Fig. 5B) was close to that of the wildtype strain on sole glucose and sole trehalose (Fig. 1B), indicating a homolactic fermentation mode in the strain Ev3. To investigate further, we simulated the metabolic fluxes of the strain Ev3 on glucose and trehalose, and found that when utilizing glucose and trehalose simultaneously the strain Ev3 performed in a similar manner as the wildtype strain on sole glucose and sole trehalose

in terms of the relative fluxes of 6-phosphofructokinase and phosphoketolase (Fig. 5C), meaning that the simultaneous utilization of carbon sources can eliminate the metabolic transition caused by the switch of carbon sources. By comparing transcriptomics data we also found either subtle (e.g. |log2FC| < 0.5) or not significant changes in expression levels of genes in the CCM between the strain Ev3 on glucose and trehalose and the wildtype strain with homolactic fermentation (SI Appendix Table S3). Altogether, the physiological, metabolic flux and gene expression data cross-confirmed that the strain Ev3 employed homolactic fermentation when co-utilizing glucose and trehalose.

We sequenced the genomes of the four evolved strains and found that the gene *crr* encoding glucose-specific phosphotransferase enzyme IIA component ($EIIA^{Glc}$) was mutated in all evolved strains (SI Appendix Table S4), in line with the findings that in various microbes the deletion of the gene *crr* diminished glucose repression on other carbon sources (47-49). In the presence of glucose, $EIIA^{Glc}$ is dephosphorylated which can inhibit transporters (50) and the genes involved in the catabolism of other carbon sources (51). By comparing the transcriptomics data between the strain Ev3 and the wildtype strain on the mixture of glucose and trehalose, we found many differentially expressed genes in the phosphotransferase system (SI Appendix Fig. S11), which might be associated with the dysfunction of $EIIA^{Glc}$.

To investigate whether the simultaneous utilization is specific to the pair of glucose and trehalose, we tested other combinations of carbon sources. We found that the strain Ev3 was also capable of co-utilizing glucose with fructose, mannose and maltose, whereas the wildtype strain employed hierarchical utilization of them (SI Appendix Fig. S12). Moreover, we found that the strain Ev3 resulted in significantly higher lactate yields on various pairs of mixed carbon sources than the wildtype strain (Fig. 5D). Therefore, the evolved strain has improved capacity of utilizing diverse types of mixed carbon sources, which could be a promising candidate for industrial fermentation where the media consist of complex carbon sources.

Discussion

Here, we observed that *B. coagulans* utilized glucose and trehalose hierarchically and transitioned from homolactic to heterolactic fermentation during the hierarchical utilization (Fig. 1). We hypothesized that the dynamic minimization of proteome reallocation might result in this observation. To test it, we reconstructed the enzyme-constrained genome-scale metabolic model of *B. coagulans*, and developed the approach of dMORP. The model with dMORP accurately simulated the transition from homolactic to heterolactic fermentation of *B. coagulans* (Fig. 2), and predicted increased reverse fluxes through glycolytic reactions (Fig. 3), which explained the noticeable reduction in the glycolytic fluxes while subtle reduction in the gene expression levels of glycolytic enzymes. Our omics data validated the model simulations: the transcriptomics and proteomics data confirmed small changes in gene expression levels of glycolytic enzymes (Fig. 4A), and the intracellular metabolite data supported the increased reverse fluxes through glycolytic reactions based on reaction thermodynamics (Fig. 4B). Moreover, we evolved strains to circumvent the hierarchical utilization and prevent the metabolic transition. Therefore, we conclude that the

dynamic minimization of proteome reallocation can explain the cellular choice of the metabolic strategies upon the change, i.e., hierarchical utilization of glucose and trehalose.

The biological basis of the minimization of proteome reallocation is the high cost and slow adjustment of protein synthesis and degradation (37,52,53) that the cells should consider when adapting to rapid perturbations. Additionally, the minimization of proteome reallocation is in line with the findings of proteome reserves (54,55), i.e., the proteome is not fully optimized for the environmental condition where the cell is living, as a suboptimal proteome could reduce the cost and time of reallocation upon the adaption to a new condition. By integrating the minimization of proteome reallocation into the constraint-based modeling framework, we developed MORP and dMORP that introduce the past proteome as an internal constraint, which provide additional objective functions for simulating cellular behaviors (56). Particularly, dMORP would serve as a promising algorithm in the field of dynamic metabolic modeling to predict cellular kinetics (57,58) and history-dependent behaviors (52,59,60).

The approach of minimization of metabolic adjustment (MOMA) has been widely used to simulate cellular behaviors in response to genetic or environmental perturbations (61-63) by minimizing the sum of absolute changes in metabolic fluxes before and after perturbations (64). Compared with minimizing the adjustment of metabolic fluxes, we argue that it is more biologically meaningful to minimize the adjustment of proteome, which now can be achieved by MORP using enzyme-constrained models. It should be noted that MORP can predict the mismatch between enzyme and flux levels caused by co-occurrence of both forward and backward fluxes of a reaction, which appears to be an impossible mission for the MOMA approach implemented on conventional GEMs. In addition, it is less computationally expensive to perform the dynamic simulations on enzyme-constrained models than on fine-grained models, such as ME-models (65,66) that explicitly formulate gene expression processes (67,25). Therefore, we expect extensive applications of MORP and dMORP with the development of enzyme-constrained models (68).

In summary, we applied systems biology approaches to decipher the principles of the cellular response of *B. coagulans* upon the hierarchical utilization of mixed carbon sources, and identified the dynamic minimization of proteome reallocation to be the cellular objective that dominates the metabolic behavior in response to rapid environmental changes. In addition, we implemented the minimization of proteome reallocation as an effective objective function in the metabolic modeling framework, which would be useful for simulating and understanding cellular responses upon perturbations.

Materials and Methods

Microorganism, media and culture conditions

B. coagulans DSM 1 = ATCC 7050 was purchased from the American Type Culture Collection.

Seed medium was MRS medium (69), simplified chemically defined medium (CDM) used for fermentation in this study, i.e., MCDM3++, which was developed in our previous study (31). 20 g/L

glucose and 20 g/L trehalose were used as the mixed carbon source to better reproduce the phenomenon of hierarchical utilization.

Seed culture and shake flask fermentation were performed in 250 mL shake flasks with 100 mL working volume at 50 ℃ and 100 rpm, pH was buffered with $CaCO_3$. The cells in seed culture were collected and washed twice using 100 mM phosphate buffer at around 12 h. Collected cells were resuspended in ultrapure water with a determined volume and then transferred to the fermentation medium in shake flasks or 5 L bioreactors. Shake flask fermentation was used to investigate the metabolic properties of different combinations of mixed carbon sources.

Batch fermentation was performed in a 5 L bioreactor with 4 L working volume at 50 °C, 100 rpm and 7.2 L/h aeration, and pH was automatically controlled at 5.5 using 25% w/v $Ca(OH)_2$. The samples of different phases were collected for determination of biomass, metabolites, transcriptome and proteome. Fermentations were performed in triplicates for all conditions.

Determination of biomass and metabolites

The optical density (OD) was detected using a spectrophotometer at 620 nm to characterize the biomass concentration.

Lactate, acetate, citate, pyruvate and acetoin in the fermentation broth were determined by high‐performance liquid chromatography (Shimadzu LC‐20AT) (12). The Hi-Plex H (300 mm × 7.7 mm) column was used with 210 nm wavelength and 50 °C column temperature; the mobile phase was 0.01 mol/L sulfuric acid solution and the flow rate was set to 0.4 mL/min.

The carbon sources in the fermentation broth were determined by ion chromatography (Dionex ICS-3000) with Dionex Carbopac PA 20 column, the method was referred to the previous description (29) and modified. The pretreatment process of the samples was performed as follows: 1) The samples were diluted to achieve sugar concentrations within the detection range. 2) $Na_2C_2O_4$ was used to precipitate calcium ions in the culture medium. 3) Proteins were removed from the samples using ethanol. 4) The processed solution was evaporated to obtain the solid form of the sugar, which was then dissolved in water to obtain the sample for testing. The mobile phase was ultrapure water and 200 mmol/L NaOH, respectively. The elution procedure was ultrapure water and 200 mmol/L NaOH eluted at 9:1 ratio for 18 min, then adjusted the ratio to 2:8 to elute for 17 min, and finally adjusted to 9:1 to balance the column for 35 min, and the flow rate for the entire process was set to 0.4 mL/min.

Reconstruction of the genome-scale metabolic model

The model iBcoa620 was reconstructed based on the model iBag597 (13): 1) A combined draft model from KEGG (70) and MetaCyc (71) pathway databases based on the genome sequences of *B. coagulans* DSM 1 = ATCC 7050 (GCF_000832905.1) was reconstructed by RAVEN 2.4.0 (72). 2) Another draft model was reconstructed by ModelSEED (73) database based on the genome annotation of RAST (74). 3) Shared reactions in the draft models were integrated with iBag597. 4) The IDs of genes, metabolites, and reactions were unified into the form of the KEGG database. 5)

Reactions with mass imbalance were corrected. 6) The memote score system was used to assess the model quality. 7) The model was validated by comparing the predicted and measure growth rates under different carbon sources.

The enzyme-constrained model eciBcoa620 was reconstructed using the GECKO 3.0 toolbox. Note that k_{cat} values were obtained from BRENDA (75) and GotEnzymes (76) databases and predicted using DLKcat tool (77). Molecular weights of all enzymes were obtained from UniProt (78) database.

MORP, dFBA and dMORP

MORP is implemented on the enzyme-constraint models, which can estimate both metabolic and enzyme usage fluxes. MORP estimates the metabolic and enzyme usage fluxes of the model upon a perturbation based on the minimization of proteome reallocation. Thus, the fluxes of the model from a reference condition should be used as the input of MORP, which can be obtained in advance by other algorithms, e.g., FBA, with the enzyme-constraint models. The core of MORP is to minimize the sum of absolute differences of enzyme usage fluxes between the reference and the perturbed conditions:

$$\min \quad \sum_{\mathrm{i}=1}^{\mathrm{m}} \left| v_{\mathrm{enzyme,i,perturb}} - v_{\mathrm{enzyme,i,ref}} \right|$$

$$\text{subject to} \quad \boldsymbol{S} \cdot \boldsymbol{v} = \boldsymbol{0}$$

$$lb_{\mathrm{j}} \leq v_{\mathrm{j}} \leq ub_{\mathrm{j}}$$

where $v_{\mathrm{enzyme,i,perturb}}$ and $v_{\mathrm{enzyme,i,ref}}$ represent fluxes of enzyme usage reaction i under perturbed and reference conditions, and m represents the total number of enzyme usage reactions in the model. As MORP estimates fluxes for the perturbed condition, $\boldsymbol{S}$ and $\boldsymbol{v}$ represent the stoichiometric matrix and flux vector of the model for the perturbed condition, and v_{j}, lb_{j} and ub_{j} are the flux, lower and upper bounds of the reaction j, respectively.

dFBA was used to simulate for the hierarchical utilization of glucose and trehalose, in which an objective function should be determined for different time intervals. As mentioned before three objective functions were used, i.e., maximization of growth, lactate production and NGAM. Generally, dFBA solves:

$$\max \quad v_{\mathrm{o,k}} \quad \mathrm{k} \in \mathrm{N}$$

$$\text{subject to} \quad \boldsymbol{S} \cdot \boldsymbol{v} = \boldsymbol{0}$$

$$v_{\mathrm{s,k}} = \frac{v_{\mathrm{s,max}}[S]_{\mathrm{k-1}}}{K_{\mathrm{m}} + [S]_{\mathrm{k-1}}}$$

$$lb_{\mathrm{j}} \leq v_{\mathrm{j}} \leq ub_{\mathrm{j}}$$

where k represents the k_{th} time interval, N represents the number of time intervals of the phase of interest and thus is a positive integer, $v_{o,k}$ is the flux of the objective reaction in P_{gluc}, i.e., the biomass formation, or the flux of the objective reaction after glucose depletion, i.e., the biomass formation, lactate production, or NGAM production, $v_{s,k}$ is the flux of the uptake reaction of the sugar, i.e., glucose or trehalose, of the kth time interval, $[S]_{k-1}$ is the sugar concentration of the $(k-1)_{th}$ time interval, $v_{s,max}$ is the maximum sugar uptake rate, and K_m is the sugar saturation constant.

dMORP was proposed to simulate the entire period after glucose depletion in the hierarchical utilization of glucose and trehalose. Here dMORP solves:

$$\min \quad \sum_{i=1}^{m} \left| v_{\mathrm{enzyme,i,r}} - v_{\mathrm{enzyme,i,r-1}} \right| \quad \mathrm{r} \in \mathrm{N}$$

$$\text{subject to} \quad \boldsymbol{S} \cdot \boldsymbol{v} = \boldsymbol{0}$$

$$v_{\mathrm{s,r}} = \frac{v_{\mathrm{s,max}}[S]_{\mathrm{r-1}}}{K_{\mathrm{m}} + [S]_{\mathrm{r-1}}}$$

$$lb_{\mathrm{j}} \leq v_{\mathrm{j}} \leq ub_{\mathrm{j}}$$

where r represents the r_{th} time interval after glucose depletion, N represents the number of time intervals of the phase of interest and thus is a positive integer, $v_{enzyme,i,r}$ and $v_{enzyme,i,r-1}$ represent the flux of enzyme usage reaction i for the r_{th} and $(r-1)_{th}$ time interval, respectively, $v_{s,r}$ is the flux of the trehalose uptake reaction of the r_{th} time interval, and $[S]_{r-1}$ is the trehalose concentration of the $(r-1)_{th}$ time interval.

All the simulations were performed with the COBRA toolbox 3.0 (80) on Matlab R2019a, and the solver was Gurobi 9.1 (https://www.gurobi.com/).

Transcriptome analysis

Cells in the fermentation broth were collected and washed three times with phosphate buffer saline for subsequent RNA extraction. Total RNA was isolated from cells using TRIzol Reagent following the instructions and genomic DNA was removed using DNase I (TaKara). Subsequently, RNA quality was determined using a Agilent2100 Bioanalyzer and quantified using ND-2000 (NanoDrop Technologies).

RNA library construction was performed using TruSeqTM RNA sample preparation Kit from Illumina (San Diego, CA). The rRNA was removed using Ribo-Zero Magnetic kit (epicenter), and double-stranded cDNA was reverse transcribed using random primers (Illumina) and SuperScript double-stranded cDNA synthesis kit (Invitrogen, CA). To synthesize the second strand of cDNA, it uses dUTP instead of dTTP, and then eliminates the second strand of cDNA containing dUTP, so that the library contained only the first strand of cDNA. After PCR amplification by Phusion DNA polymerase (NEB) and TBS380 (Picogreen) quantification, paired-end RNA-seq sequencing library was sequenced with the Illumina Novaseq (2 × 150bp read length).

The data generated from Illumina platform were used for bioinformatics analysis, and the reference genome and gene annotation files of *B. coagulans* DSM 1 = ATCC 7050 were downloaded from the National Center for Biotechnology Information. All of the analyses were performed using the free online platform of Majorbio Cloud Platform (www.majorbio.com).

Proteome analysis

Cells in the fermentation broth were collected and washed three times with phosphate buffer saline for subsequent protein extraction. Sample lysis and protein extraction were performed using SDT (4% SDS, 100 mM Tris-HCl, 1 mM DTT, pH 7.6) buffer, and the protein was quantified using the BCA Protein Assay Kit (Bio-Rad, USA). Protein digestion was performed with trypsin following the filter-aided sample preparation (FASP) procedure. The digested peptides from each sample were subsequently desalted (Empore™ SPE Cartridges C18 (standard density), bed I.D. 7 mm, volume 3 mL, Sigma) and concentrated. The protein for each sample were quantified by SDS-PAGE. 100 μg peptide mixture for each sample was labeled using TMT reagent according to the instructions (Thermo Scientific). The labeled peptides were separated by High pH Reversed-Phase Peptide Fractionation Kit (Thermo Scientific) to obtain 10 different fractions, the collected fractions were desalted on C18 Cartridges and concentrated.

LC-MS/MS analysis was performed using a Thermo Scientific Q Exactive mass spectrometer equipped with the Easy nLC system (Proxeon Biosystems, Thermo Fisher Scientific). Peptides were trapped on a reverse phase trap column (Thermo Scientific Acclaim PepMap100, 100 μm × 2 cm, nanoViper C18) and separated on the C18-reversed phase analytical column (Thermo Scientific Easy Column, 10 cm long, 75 μm inner diameter, 3 μm resin). The separation was achieved using buffer A (0.1% formic acid) and buffer B (84% acetonitrile and 0.1% formic acid) at a constant flow rate of 300 nL/min controlled by IntelliFlow technology. The mass spectrometer was operated in positive ion mode. MS/MS analysis was performed using the data-dependent top10 method for high-energy collision dissociation (HCD) fragmentation by selecting the most abundant precursor ion (300-1800 m/z) in the measurement scan. The MS raw data was subjected to identification and quantitative analysis using MASCOT engine (Matrix Science, London, UK; version 2.2) and Proteome Discoverer 1.4 software. The proteome detection and analysis process were conducted in shanghai applied protein technology co.ltd.

Determination of intracellular metabolites

The absolute quantification of intracellular phosphate sugars, organic acids, and amino acids was performed using gas chromatography-mass spectrometry (Agilent, GC-7890A, MS-5975C). Before the extraction of intracellular metabolites, a quenching step was performed to terminate cell metabolism. 2 mL of fermentation broth were added to a 50 mL centrifuge tube containing 30 mL of 60% methanol pre-cooled to -27 °C. After quenching for 5 minutes, filter paper with attached cells was obtained by filtration. Simultaneously, 100 μL of U-13C-labeled cell extracts was added to the filter paper as internal standards. The filter paper was then placed in a 75% ethanol solution pre-heated to 80 °C and boiled for 5 min. The filter paper was removed, and the remaining liquid was concentrated to 600 μL using rapid evaporation. A 100 μL portion was taken as the sample and subjected to freeze-drying before derivatization (13,81,82).

Amino acids derivatization method: 100 μL of pyridine was added to the freeze-dried sample, and the mixture was dissolved in a 65 °C for 1 hour. After the sample reached room temperature, 100 μL of derivatization reagent (N - tert - butyldimethylsilyl - N-methyl-trifluoroacetamide with 1% tert - butyldimethylchlorosilane) was added, and derivatization was carried out in a 65 °C oven for 1 hour. The sample was then centrifuged at 12000 rpm for 5 min, and the supernatant was subjected to GC-MS analysis.

Phosphate sugars and organic acids derivatization method: 50 μL of 20 mg/mL methoxyamine pyridine solution was added to the freeze-dried sample. The mixture was dissolved in a 65 °C oven for 1 hour. After reaching room temperature, 80 μL of N-methyl-N-(trimethylsilyl) trifluoroacetamide/trimethylchlorosilane (MSTFA/TMCS, 1000:50, v/v) was added, and derivatization was carried out in a 65 ℃ oven for 1 hour. The sample was then centrifuged at 12000 rpm for 5 minutes, and the supernatant was subjected to GC-MS analysis.

The GC-MS detection conditions were as follows: the interface temperature of the GC-MS was set at 280 °C, the transfer line temperature was 250 °C, Ionization was done by electron impact with the temperature being 230 °C, the quadrupole temperature was 150 °C, and the injection volume was 1 μL. The chromatographic column used was HP-5MS with dimensions of 30 mm × 0.25 mm × 0.25 μm. For amino acids, the temperature program consisted of an initial column temperature of 100 °C for 1 minute, followed by an increase at a rate of 10 °C/min to reach 320 °C, which was then maintained for 10 minutes. For phosphate sugars and organic acids, the temperature program started with an initial column temperature of 70 °C for 1 minute, followed by an increase at a rate of 10 °C/min to reach 300 °C, which was then maintained for 10 minutes.

Adaptive laboratory evolution

The adaptive laboratory evolution strategy was performed in a 250 mL shake flask with complex medium, 100 rpm, 50 °C. Alternating cultures of glucose and trehalose were utilized, while the trehalose was supplemented with glucose structural analogue (2-deoxy-D-glucose), which can be absorbed but not be metabolized, so it can be used for screening mutant strains without catabolite repression effect (83,84). The hope was to obtain strains that could utilize glucose and trehalose simultaneously. During the evolution process, the cells were transferred to new medium in the exponential phase and maintained the same concentration (OD620 about 0.5) after inoculation. The initial total sugar concentration during evolution was kept constant at 130 g/L (glucose 130 g/L, 2-deoxy-D-glucose 40 g/L + trehalose 90 g/L), and the concentration of 2-deoxy-D-glucose was determined according to our previous study. Four evolved strains with the expected phenotypes were examined by MRS plate culture, and the strain with faster sugar consumption rate and higher lactate yield was selected for fermentation experiments in 5 L bioreactor.

Whole-genome sequencing

Cells from the exponential phase in seed shake flasks were collected for genome sequencing. Genomic DNA of *B. coagulans* DSM 1 = ATCC 7050 was extracted using Wizard Genomic DNA Purification Kit (Promega) according to the protocol. Purified genomic DNA was quantified by TBS-

380 fluorometer (Turner BioSystems Inc., Sunnyvale, CA). Whole-genome sequencing of wildtype strain and four evolved strains was performed using the de novo sequencing method based on the Illumina NovaSeq6000 platform in this study. The final genome of five strains were annotated from KEGG, GO, COG and other databases using BLASTP, Diamond and HMMER. The same mutated genes of four evolved strains were considered to be genes that could cause phenotypic change.

Data availability

The genome sequences of four evolved strains have been deposited in NCBI database under the BioProject accession number of PRJNA1012373. The transcriptomics data have been deposited in NCBI database under the BioProject accession number of PRJNA1012495. The mass spectrometry proteomics datasets have been deposited in the ProteomeXchange with the dataset identifier PXD045169.

Code availability

The models and code are available at https://github.com/ChenYuGroup/MORP.

Acknowledgments

This study was financially supported by the National Key Research and Development Program of China (2023YFA0913900), the Shenzhen Medical Research Fund (A2303026) and the National Natural Science Foundation of China (21878084).

Author Contributions: Y.C., Y.W. and Z.L. conceived the study. Z.L., M.C. and J.H. performed the experiments. Z.L. and Y.C. constructed the models and performed the simulations. Z.L. and Y.C. analyzed the data. Y.C., Z.L. and Y.W. wrote the paper. All authors approved the final paper.

Competing Interest: The authors declare no competing interests.

References

1. M. G. Vander Heiden, L. C. Cantley, C. B. Thompson, Understanding the Warburg effect: the metabolic requirements of cell proliferation. *Science* 2009, 324(5930): 1029-1033.
2. M. Basan *et al.*, Overflow metabolism in *Escherichia coli* results from efficient proteome allocation. *Nature* 528(7580): 99-104 (2015).
3. B. Niebel, S. Leupold, M. Heinemann, An upper limit on Gibbs energy dissipation governs cellular metabolism. *Nat. Metab.* 1(1): 125-132 (2019).
4. Y. Shen *et al.*, Proteome capacity constraints favor respiratory ATP generation. *bioRxiv* 2022.08. 10.503479 (2022).
5. T. Pfeiffer, S. Schuster, S. Bonhoeffer, Cooperation and competition in the evolution of ATP-producing pathways. *Science* 292(5516): 504-507 (2001).
6. D. Molenaar, R. Van Berlo, D. De Ridder, B. Teusink, Shifts in growth strategies reflect tradeoffs in cellular economics. *Mol. Syst. Biol.* 5(1): 323 (2009).
7. A. Flamholz, E. Noor, A. Bar-Even, W. Liebermeister, R. Milo, Glycolytic strategy as a tradeoff between energy yield and protein cost. *Proc. Natl. Acad. Sci. U.S.A.* 110(24): 10039-10044 (2013).
8. M. Szenk, K. A. Dill, A. M. R. de Graff, Why do fast-growing bacteria enter overflow metabolism? Testing the membrane real estate hypothesis. *Cell Syst.* 5(2): 95-104 (2017).

9. B. Du, D. C. Zielinski, J. M. Monk, B. O. Palsson, Thermodynamic favorability and pathway yield as evolutionary tradeoffs in biosynthetic pathway choice. *Proc. Natl. Acad. Sci. U.S.A.* 115(44): 11339-11344 (2018).
10. Y. Chen, J. Nielsen, Energy metabolism controls phenotypes by protein efficiency and allocation. *Proc. Natl. Acad. Sci. U.S.A.* 116(35): 17592-17597 (2019).
11. R. Schuetz, N. Zamboni, M. Zampieri, U. Sauer, Multidimensional optimality of microbial metabolism. *Science* 336(6081): 601-604 (2012).
12. X. Lv *et al.*, Effect of pH, glucoamylase, pullulanase and invertase addition on the degradation of residual sugar in L-lactic acid fermentation by *Bacillus coagulans* HL-5 with corn flour hydrolysate. *J. Taiwan Inst. Chem. Eng.* 61, 124-131 (2016).
13. Y. Chen *et al.*, Genome-scale modeling for *Bacillus coagulans* to understand the metabolic characteristics. *Biotechnol. Bioeng.* 117, 3545-3558 (2020).
14. M. G. Gänzle, Lactic metabolism revisited: metabolism of lactic acid bacteria in food fermentations and food spoilage. *Curr. Opin. Food Sci.* 2, 106-117 (2015).
15. Y. Wang *et al.*, Metabolism characteristics of lactic acid bacteria and the expanding applications in food industry. *Front. Bioeng. Biotechnol.* 9: 612285 (2021).
16. Q. Wang, L. O. Ingram, K. Shanmugam, Evolution of D-lactate dehydrogenase activity from glycerol dehydrogenase and its utility for D-lactate production from lignocellulose. *Proc. Natl Acad. Sci. U.S.A.* 108, 18920-18925 (2011).
17. L. Wang *et al.*, Jerusalem artichoke powder: a useful material in producing high-optical-purity L-lactate using an efficient sugar-utilizing thermophilic *Bacillus coagulans* strain. *Bioresour. Technol.* 130, 174-180 (2013).
18. M. A. Abdel-Rahman, Y. Tashiro, K. Sonomoto, Recent advances in lactic acid production by microbial fermentation processes. *Biotechnol. Adv.* 31, 877-902 (2013).
19. Z. Lu, F. He, Y. Shi, M. Lu, L. Yu, Fermentative production of L (+)-lactic acid using hydrolyzed acorn starch, persimmon juice and wheat bran hydrolysate as nutrients. *Bioresour. Technol.* 101, 3642-3648 (2010).
20. R. Hermsen, H. Okano, C. You, N. Werner, T. Hwa, A growth-rate composition formula for the growth of *E. coli* on co-utilized carbon substrates. *Mol. Syst. Biol.* 11, 801 (2015).
21. E. Perrin *et al.*, Diauxie and co-utilization of carbon sources can coexist during bacterial growth in nutritionally complex environments. *Nat. Commun.* 11, 3135 (2020).
22. H. Okano, R. Hermsen, T. Hwa, Hierarchical and simultaneous utilization of carbon substrates: mechanistic insights, physiological roles, and ecological consequences. *Curr. Opin. Microbiol.* 63, 172-178 (2021).
23. A. Solopova *et al.*, Bet-hedging during bacterial diauxic shift. *Proc. Natl Acad. Sci. U.S.A.* 111, 7427-7432 (2014).
24. H. Okano, R. Hermsen, K. Kochanowski, T. Hwa, Regulation underlying hierarchical and simultaneous utilization of carbon substrates by flux sensors in *Escherichia coli*. *Nat. Microbiol.* 5, 206-215 (2020).
25. P. Salvy, V. Hatzimanikatis, Emergence of diauxie as an optimal growth strategy under resource allocation constraints in cellular metabolism. *Proc. Natl Acad. Sci. U.S.A.* 118, e2013836118 (2021).
26. C. Sievert *et al.*, Experimental evolution reveals an effective avenue to release catabolite repression via mutations in XylR. *Proc. Natl Acad. Sci. U.S.A.* 114, 7349-7354 (2017).
27. P. Gawand, P. Hyland, A. Ekins, V. J. Martin, R. Mahadevan, Novel approach to engineer strains for simultaneous sugar utilization. *Metab. Eng.* 20, 63-72 (2013).
28. K. Ma *et al.*, Highly efficient production of optically pure L-lactic acid from corn stover hydrolysate by thermophilic *Bacillus coagulans*. *Bioresour. Technol.* 219, 114-122 (2016).
29. X. Lv, Y. Guo, Y. Zhuang, Y. Wang, Optimization and validation of an extraction method and HPAEC-PAD for determination of residual sugar composition in L-lactic acid industrial fermentation broth with a high salt content. *Anal. Methods* 7, 9076-9083 (2015).
30. Y. J. Wee, J. S. Yun, D. H. Park, H. W. Ryu, Isolation and characterization of a novel lactic acid bacterium for the production of lactic acid. *Biotechnol. Bioprocess Eng.* 9, 303-308 (2004).

31. Y. Chen, F. Dong, Y. Wang, Systematic development and optimization of chemically defined medium supporting high cell density growth of *Bacillus coagulans*. Appl. *Microbiol. Biotechnol.* 100, 8121-8134 (2016).
32. C. Lieven *et al.*, MEMOTE for standardized genome-scale metabolic model testing. *Nat. Biotechnol.* 38, 272-276 (2020).
33. Y. Chen *et al.*, Reconstruction, simulation and analysis of enzyme-constrained metabolic models using GECKO Toolbox 3.0. *Nat. Protoc.* 1-39 (2024).
34. J. D. Orth, I. Thiele, B. O. Palsson, What is flux balance analysis?. *Nat. Biotechnol.* 28, 245-248 (2010).
35. D. Henriques *et al.*, A multiphase multiobjective dynamic genome-scale model shows different redox balancing among yeast species of the *Saccharomyces* genus in fermentation. *mSystems* 6, e00260-21 (2021).
36. M. Kafri, E. Metzl-Raz, G. Jona, N. Barkai, The cost of protein production. *Cell Reports* 14, 22-31 (2016).
37. E. Noor *et al.*, Pathway thermodynamics highlights kinetic obstacles in central metabolism. *PLoS Comput. Biol.* 10, e1003483 (2014).
38. J. Xu *et al.*, Metabolic flux analysis and fluxomics-driven determination of reaction free energy using multiple isotopes. *Curr. Opin. Biotechnol.* 64: 151-160 (2020).
39. J. O. Park *et al.*, Metabolite concentrations, fluxes and free energies imply efficient enzyme usage. *Nat. Chem. Biol.* 12(7): 482-489 (2016).
40. P. Grigaitis, B. Teusink, An excess of glycolytic enzymes under glucose-limited conditions may enable Saccharomyces cerevisiae to adapt to nutrient availability. *FEBS Lett.* 596(24): 3203-3210 (2022).
41. L. Gerosa *et al.*, Pseudo-transition analysis identifies the key regulators of dynamic metabolic adaptations from steady-state data. *Cell Syst.* 1, 270-282 (2015).
42. D. Davidia *et al.*, Global characterization of in vivo enzyme catalytic rates and their correspondence to in vitro k_{cat} measurements. *Proc. Natl Acad. Sci. U.S.A.* 113, 3401-3406 (2016).
43. S. Zhao *et al.*, Regulation of cellular metabolism by protein lysine acetylation. *Science* 327, 1000-1004 (2010).
44. M. I. Espinosa *et al.*, Adaptive laboratory evolution of native methanol assimilation in Saccharomyces cerevisiae. *Nat. Commun.* 11, 5564 (2020).
45. D. Choe *et al.*, S. C. Kim, B. K. Cho, Adaptive laboratory evolution of a genome-reduced Escherichia coli. *Nat. Commun.* 10, 935 (2019).
46. B. R. Oh *et al.*, The production of 1, 3-propanediol from mixtures of glycerol and glucose by a Klebsiella pneumoniae mutant deficient in carbon catabolite repression. *Bioresour. Technol.* 130, 719-724 (2013).
47. M. Zhao, D. Shi, X. Lu, H. Zong, B. Zhuge, Co-production of 1, 2, 4-butantriol and ethanol from lignocellulose hydrolysates. *Bioresour. Technol.* 282, 433-438 (2019).
48. Q. Liang *et al.*, Comparison of individual component deletions in a glucose-specific phosphotransferase system revealed their different applications. *Sci Rep* 5, 13200 (2015).
49. B. Görke, J. Stülke, Carbon catabolite repression in bacteria: many ways to make the most out of nutrients. *Nat. Rev. Microbiol.* 6, 613-624 (2008).
50. A. Nair, S. J. Sarma, The impact of carbon and nitrogen catabolite repression in microorganisms. *Microbiol. Res.* 251, 126831 (2021).
51. D. L. Rothman, P. B. Moore, R. G. Shulman, The impact of metabolism on the adaptation of organisms to environmental change. *Front. Cell. Dev. Biol.* 11, 1197226 (2023).
52. M. Scott, T. Hwa, Shaping bacterial gene expression by physiological and proteome allocation constraints. *Nat. Rev. Microbiol.* 21, 327-342 (2023).
53. C. Wu *et al.*, Enzyme expression kinetics by *Escherichia coli* during transition from rich to minimal media depends on proteome reserves. *Nat. Microbiol.* 8(2): 347-359 (2023).
54. R. Yu *et al.*, Nitrogen limitation reveals large reserves in metabolic and translational capacities of yeast. *Nat. Commun.* 11(1): 1881 (2020).

55. D. B. Bernstein, S. Sulheim, E. Almaas, D. Segrè, Addressing uncertainty in genome-scale metabolic model reconstruction and analysis. *Genome Biol.* 22: 1-22 (2021).
56. D. W. Erickson *et al.*, A global resource allocation strategy governs growth transition kinetics of *Escherichia coli*. *Nature* 551, 119-123 (2017).
57. M. Basan *et al.*, A universal trade-off between growth and lag in fluctuating environments. *Nature* 584, 470-474 (2020).
58. B. Cerulus *et al.*, Transition between fermentation and respiration determines history-dependent behavior in fluctuating carbon sources. *eLife* 7: e39234 (2018).
59. L. Vermeersch *et al.*, Do microbes have a memory? History-dependent behavior in the adaptation to variable environments. *Front. Microbiol.* 13: 1004488 (2022).
60. J. S. L. Yu *et al.*, Microbial communities form rich extracellular metabolomes that foster metabolic interactions and promote drug tolerance. *Nat. Microbiol.* 7, 542-555 (2022).
61. W. C. Ho, J. Zhang, Evolutionary adaptations to new environments generally reverse plastic phenotypic changes. *Nat. Commun.* 9, 350 (2018).
62. S. Vaud *et al.*, Engineering improved ethylene production: Leveraging systems biology and adaptive laboratory evolution. *Metab. Eng.* 67, 308-320 (2021).
63. D. Segre, D. Vitkup, G. M. Church, Analysis of optimality in natural and perturbed metabolic networks. *Proc. Natl Acad. Sci. U.S.A.* 99, 15112-15117 (2002).
64. C.J. Lloyd *et al.*, COBRAme: A computational framework for genome-scale models of metabolism and gene expression. *PLoS Comput. Biol.* 14, e1006302 (2018).
65. A.M. Reimers, H. Knoop, A. Bockmayr, R. Steuer, Cellular trade-offs and optimal resource allocation during cyanobacterial diurnal growth. *Proc. Natl Acad. Sci. U.S.A.* 114(31): E6457-E6465 (2017).
66. L. Yang, A. Ebrahim, C. J. Lloyd, M. A. Saunders, B. O. Palsson, DynamicME: dynamic simulation and refinement of integrated models of metabolism and protein expression. *BMC Syst. Biol.* 13, 1-15 (2019).
67. Y. Chen, J. Nielsen, Mathematical modeling of proteome constraints within metabolism. *Curr. Opin. Syst. Biol.* 25, 50-56 (2021).
68. A. N. David, Y. Sewsynker-Sukai, E. G. Kana, Co-valorization of corn cobs and dairy wastewater for simultaneous saccharification and lactic acid production: Process optimization and kinetic assessment. *Bioresour. Technol.* 348, 126815 (2022).
69. M. Kanehisa, S. Goto, KEGG: kyoto encyclopedia of genes and genomes. *Nucleic Acids Res.* 28, 27-30 (2000).
70. P. D. Karp, M. Riley, S. M. Paley, A. Pellegrini-Toole, The metacyc database. *Nucleic Acids Res.* 30, 59-61 (2002).
71. H. Wang *et al.*, RAVEN 2.0: A versatile toolbox for metabolic network reconstruction and a case study on *Streptomyces coelicolor*. *PLoS Comput. Biol.* 14, e1006541 (2018).
72. C.S. Henry *et al.*, High-throughput generation, optimization and analysis of genome-scale metabolic models. *Nat. Biotechnol.* 28, 977-982 (2010).
73. R. K. Aziz *et al.*, The RAST Server: rapid annotations using subsystems technology. *BMC genomics* 9, 1-15 (2008).
74. L. Jeske, S. Placzek, I. Schomburg, A. Chang, D. Schomburg, BRENDA in 2019: a European ELIXIR core data resource. *Nucleic Acids Res.* 47, D542-D549 (2019).
75. F. Li, Y. Chen, M. Anton, J. Nielsen, GotEnzymes: an extensive database of enzyme parameter predictions. *Nucleic Acids Res.* 51, D583-D586 (2023).
76. F. Li *et al.*, Deep learning-based k_{cat} prediction enables improved enzyme-constrained model reconstruction. *Nat. Catal.* 5, 662-672 (2022).
77. R. Apweiler *et al.*, UniProt: the universal protein knowledgebase. *Nucleic Acids Res.* 32, D115-D119 (2004).
78. N. E. Lewis *et al.*, Omic data from evolved *E. coli* are consistent with computed optimal growth from genome-scale models. *Mol. Syst. Biol.* 6, 390 (2010).
79. L. Heirendt *et al.*, Creation and analysis of biochemical constraint-based models using the COBRA Toolbox v. 3.0. *Nat. Protoc.* 14, 639-702 (2019).

80. G. Wang, J. Chu, Y. Zhuang, W. van Gulik, H. Noorman, A dynamic model-based preparation of uniformly-13C-labeled internal standards facilitates quantitative metabolomics analysis of *Penicillium chrysogenum*. *J. Biotechnol.* 299, 21-31 (2019).
81. X. Liu *et al.*, Dynamic changes of metabolomics and expression of candicidin biosynthesis gene cluster caused by the presence of a pleiotropic regulator AdpA in *Streptomyces* ZYJ-6. Bioprocess. *Biosyst. Eng.* 42, 1353-1365 (2019).
82. J. Liang, R. van Kranenburg, A. Bolhuis, D. J. Leak, Removing carbon catabolite repression in *Parageobacillus thermoglucosidasius* DSM 2542. *Front. Microbiol.* 13, 985465 (2022).
83. A. Veyrat, V. Monedero, G. Perez-Martinez, Glucose transport by the phosphoenolpyruvate: mannose phosphotransferase system in *Lactobacillus casei* ATCC 393 and its role in carbon catabolite repression. *Microbiology* 140, 1141-1149 (1994).